

Golden and Silver Dark Sirens for precise H_0 measurement with HETDEX

YIXUAN DANG ^{1,2} ISH GUPTA ^{1,3,4,5} ROBIN CIARDULLO ^{6,1} ERIN MENTUCH COOPER ⁷ SHIKSHA PANDEY ¹,
 DUSTIN DAVIS ,⁷ SURHUD MORE ,⁸ RACHEL GRAY ,⁹ HSIN-YU CHEN ,¹⁰ DANIEL J. FARROW ,^{11,12}
 CARYL GRONWALL ,^{6,1} DONGHUI JEONG ,^{6,1} SHUN SAITO ,^{13,14} DONALD P. SCHNEIDER ,^{6,1} AND
 B. S. SATHYAPRAKASH 

¹ *Institute for Gravitation and the Cosmos, The Pennsylvania State University, University Park, PA 16802, USA*

² *Department of Physics, The Pennsylvania State University, University Park, PA 16802, USA*

³ *Department of Physics, University of California, Berkeley, CA 94720, USA*

⁴ *Department of Physics and Astronomy, Northwestern University, 2145 Sheridan Road, Evanston, IL 60208, USA*

⁵ *Center for Interdisciplinary Exploration and Research in Astrophysics (CIERA), Northwestern University, 1800 Sherman Ave, Evanston, IL 60201, USA*

⁶ *Department of Astronomy & Astrophysics, The Pennsylvania State University, University Park, PA 16802, USA*

⁷ *Department of Astronomy, The University of Texas at Austin, 2515 Speedway Boulevard, Austin, TX 78712, USA*

⁸ *Inter-University Centre for Astronomy and Astrophysics, Pune, Maharashtra 411007, India*

⁹ *SUPA, University of Glasgow, Glasgow, G12 8QQ, United Kingdom*

¹⁰ *Department of Physics, The University of Texas at Austin, 2515 Speedway, Austin, TX 78712, USA*

¹¹ *E. A. Milne Centre for Astrophysics University of Hull, Cottingham Road, Hull, HU6 7RX, UK*

¹² *Centre of Excellence for Data Science, Artificial Intelligence & Modelling (DAIM), University of Hull, Cottingham Road, Hull, HU6 7RX, UK*

¹³ *Institute for Multi-messenger Astrophysics and Cosmology, Department of Physics, Missouri University of Science and Technology, 1315 N Pine Street, Rolla, MO 65409, USA*

¹⁴ *Kavli Institute for the Physics and Mathematics of the Universe (Kavli IPMU, WPI), University of Tokyo, Chiba 277-8582, Japan*

ABSTRACT

Gravitational waves (GWs) from compact binary coalescences are *standard sirens* that provide a direct measure of the source’s luminosity distance, enabling an independent measurement of the Hubble constant (H_0). While a *bright siren*—a GW event with an identified electromagnetic (EM) counterpart—provided the first such constraint, most detections, currently dominated by black hole mergers, lack EM signatures. A measurement of H_0 is still possible with these *dark sirens* by statistically associating GW events with galaxies in existing catalogs based on the sky localization. In this work, we explore the potential of two subsets of sirens: rare *golden* dark sirens, for which a single galaxy dominates the H_0 posterior, and *silver* dark sirens, which are far more common but have a larger set of plausible host galaxies. Using the *fifth internal data release* of the Hobby–Eberly Telescope Dark Energy Experiment (HETDEX), we assess the suitability of the Visible Integral-field Replicable Unit Spectrograph (VIRUS) for spectroscopic follow-up of dark sirens. VIRUS exposures of the standard HETDEX depth provide precise redshifts and exquisite completeness within $z = 0.2$. After a single year of observations with the upgraded LIGO–A[#] network, the combined sample of golden and silver dark sirens with $z \leq 0.2$ and follow-up VIRUS observations can potentially yield a few-percent constraint on H_0 . Our predictions suggest that spectroscopic redshift surveys such as HETDEX can play a key role in realizing high-precision cosmology with dark sirens in the near future. Standard-siren distance measurements offer a critical, fully independent path to the local value of H_0 to resolve the Hubble tension.

Keywords: Gravitational waves (678) — Cosmology (343) — Hubble constant (758)

1. INTRODUCTION

Email: ykd5167@psu.edu

It is remarkable, and deeply troubling that a century after Edwin Hubble’s discovery of the expansion of the

universe, we still lack a precise and consistent determination of the rate of this expansion. The Hubble tension (e.g., L. Verde et al. 2019; E. Di Valentino et al. 2025)—the $4\text{-}6\sigma$ discrepancy between the Planck Cosmic Microwave Background (CMB) value of the Hubble Constant (N. Aghanim et al. 2020) and the local value of H_0 measured from the Supernova H_0 for the Equation of State of Dark Energy (SH0ES) program (e.g., A. G. Riess et al. 2022; A. G. Riess et al. 2025)—is one of the most pressing challenges in modern physics. The mismatch indicates either the presence of unknown systematics in the measurements or the existence of new physics (V. Poulin et al. 2019; E. Di Valentino et al. 2019, 2021, 2025).

Gravitational waves (GWs) from compact binary coalescences (CBCs) provide a direct measurement of the source’s luminosity distance, making them powerful *standard sirens* for independent determinations of H_0 (B. F. Schutz 1986; D. E. Holz & S. A. Hughes 2005). So-called *bright sirens* constrain H_0 by allowing the direct detection of the event’s electromagnetic (EM) counterpart and yield an unambiguous redshift for the source. This approach was first demonstrated by the binary neutron star (BNS) merger GW170817 (T. L. S. Collaboration et al. 2015; B. P. Abbott et al. 2017a) via the optical transient discovered near its host galaxy NGC 4993 (B. P. Abbott et al. 2017b). However, since GW170817, only one additional BNS event and a few neutron star–black hole (NSBH) mergers have been detected (A. G. Abac et al. 2025), none with a confirmed EM counterpart. The detectability of such counterparts depends on the intrinsic merger rate, the neutron-star equation of state (EoS), and the ability to localize and follow up events in a timely manner. While studies suggest that next-generation detectors could routinely identify BNS and NSBH mergers (M. Bailes et al. 2021; M. Branchesi et al. 2023), the number of events with observable counterparts is expected to remain small due to the small fraction of events with favorable source geometry (i.e., close to face-on or face-off systems), low merger rate (R. Abbott et al. 2023; A. G. Abac et al. 2025) and potentially soft EoS (C. Palenzuela et al. 2015).

Fortunately, measurements of H_0 with GW sources are still possible despite the lack of EM counterparts. The statistical or dark-siren method (B. F. Schutz 1986; J. R. Gair et al. 2023; R. Gray 2021; R. Gray et al. 2020) identifies potential host galaxies of CBCs by combining the GW sky localization with galaxy redshifts from existing spectroscopic or photometric catalogs (e.g., G. Dálya et al. 2018, 2022). In this approach, all galaxies consistent with the GW localization are weighted by their probability of hosting the merger, and the resulting

redshift distribution is combined with the GW-inferred luminosity distance to obtain a posterior on H_0 . One advantage of this approach is that rapid EM follow-up is not required; galaxy redshifts can be obtained well-after the time of the event.

Another approach—the spectral-siren method—uses population-level features in the *source-frame mass distribution* of compact binaries (S. R. Taylor & J. R. Gair 2012; S. Mastrogiovanni et al. 2021; J. M. Ezquiaga & D. E. Holz 2022). Here “source-frame mass” refers to the true physical masses of the binary components, before cosmological redshift stretches the GW frequency and causes the *detector-frame masses* to appear larger. Because GW detectors measure only redshifted masses, a mass–redshift degeneracy arises: a distant system with lower intrinsic masses can mimic a nearby system with higher mass components. Population-level modeling of the intrinsic mass distribution can partially break this degeneracy and thereby constrain H_0 . Other methods that use GW observations to infer the Hubble constant include the stochastic-siren technique (B. Cousins et al. 2025), and the cross-correlation of GW sources with the large-scale distribution of galaxies (T. Namikawa et al. 2016; S. Mukherjee et al. 2020, 2021; S. Bera et al. 2020; S. Mukherjee et al. 2024; S. Afroz & S. Mukherjee 2024).

In this paper, we focus on two subclasses of dark sirens: (1) *golden dark sirens* (S. Borhanian et al. 2020; I. Gupta 2023; A. Chen 2025), for which only a single cataloged galaxy is a plausible host, and (2) *silver dark sirens*, for which multiple galaxies within a redshift catalog could potentially host the source. For the purpose of planning for EM observations, we adopt a practical observational classification: any GW event with a 90% credible sky area smaller than 0.1 deg^2 is designated as a *golden* dark siren, while those with a 90% area below 1 deg^2 are classified as *silver* dark sirens. The advantage of these designations is that the classification is based on the GWs themselves, as the true number of potential host galaxies is unknown until dedicated follow-up observations are performed.

Since both golden and silver dark sirens rely heavily on knowing the redshifts of the potential host galaxies near the position of the GW event, it is important to have a catalog that ensures a nearly complete detection of objects in the expected volume. Moreover, previous works have established that for well-localized events (e.g., $\Delta\Omega_{90} \approx 1 \text{ deg}^2$), spectroscopic redshifts offer a 15% better constraint on H_0 compared to photometric redshifts (M. L. Cross-Parkin et al. 2025). Therefore, to fully exploit the potential of dark sirens, it is necessary to identify a facility capable of obtaining deep spectroscopy of all possible hosts of a GW event. The Visi-

ble Integral-field Replicable Unit Spectrograph (VIRUS; G. J. Hill et al. 2021) on the Hobby-Eberly Telescope (HET; L. W. Ramsey et al. 1998) is an ideal instrument for dark siren follow-up. The Hobby-Eberly Telescope Dark Energy Experiment (HETDEX; K. Gebhardt et al. 2021) illustrates the power of VIRUS, as the instrument has recently been used to measure large scale structure over 540 deg^2 of the $1.9 < z < 3.5$ universe. In this work, we explore the potential of constructing HETDEX-style surveys for golden and silver dark sirens. Such a dedicated spectroscopic follow-up strategy has already been demonstrated for one well-localized dark siren event (H. Zhang et al. 2025), motivating a systematic exploration for optimizing future observations.

The rest of the paper is structured as follows: In Section 2 we introduce the idea of building event-specific catalogs with the HET to accomplish the measurements required for GW sources detected with a network consisting of LIGO, Virgo and LIGO-India observatories. This analysis validates the EM follow-up strategy. Section 3 presents the statistical framework used for the H_0 analysis performed, together with potential systematic effects and their mitigation. In Section 4 we describe the specific models and data; Sections 5 and 6 present results and conclusions.

2. TOWARD EVENT-SPECIFIC CATALOGS

In this section, we outline the observational and detector requirements needed to construct *event-specific* spectroscopic catalogs for well-localized GW sources. We first describe the capabilities of the Hobby-Eberly Telescope and the VIRUS integral-field spectrograph, which together provide the depth and completeness necessary for galaxy redshift follow-up over degree-scale localization regions. We then summarize the GW detector networks and sensitivity configurations assumed throughout this work, and finally validate the proposed EM follow-up strategy by quantifying the expected number of golden and silver dark sirens, the suitability of HETDEX-style observations, and the resulting constraints on H_0 .

2.1. VIRUS on the Hobby-Eberly Telescope

One of the most used instruments on the Hobby-Eberly Telescope is VIRUS, a low-resolution integral-field unit (IFU) spectrograph designed for wide-field surveys. Since it is an IFU spectrograph, VIRUS records the spectrum of every object falling onto its field of view without any pre-selection, and, since the instrument is coupled to a 10-m class telescope, redshifts well-beyond $z \sim 0.2$ can be accurately measured with exposure times of $\lesssim 20$ minutes. Most importantly, VIRUS has the

widest field-of-view of any IFU in existence, covering more than 55 arcmin^2 in a single observation. It is therefore capable of surveying the entire 1 deg^2 sky area of a silver siren in ~ 60 pointings.

The fifth internal data release of HETDEX (E. Mentuch Cooper et al. 2023) is particularly useful for exploring the utility of VIRUS for standard siren investigations. Although this database is primarily designed to identify emission lines brighter than $\sim 5 \times 10^{-17} \text{ ergs cm}^{-2} \text{ s}^{-1}$ via the Emission Line eXplorer classification tool (ELiXeR; D. Davis et al. 2023), it also contains continuum-based redshifts for sources brighter than $g \sim 23$ via the Diagnose spectral classification package (G. R. Zeimann et al. 2024). Roughly speaking, in just ~ 21 hours of exposure time, VIRUS can survey the entire 1 deg^2 localization area of a silver GW source at $z = 0.2$ and obtain a $\lesssim 0.15\%$ precision radial velocity for every potential host having a continuum luminosity more than half that of the Large Magellanic Cloud, or a star formation rate more than a tenth that of the Milky Way (K. Gebhardt et al. 2021; K. Hawkins et al. 2021; G. R. Zeimann et al. 2024). In Section 4.2 we use the HETDEX catalog to examine this claim and conclude that, indeed, any effect on H_0 due to incompleteness in the catalog is negligible. This capability allows one to ignore most EM selection effects in our preliminary H_0 forecast.

2.2. LIGO, Virgo and LIGO-India Detector Networks

Next, we present a quantitative framework for designing HETDEX-style, event-specific spectroscopic surveys tailored to the golden and silver dark sirens expected from future ground-based GW detector networks. These networks will consist of upgraded versions of the currently operating LIGO and Virgo detectors, together with LIGO-India, which is now under construction. In our analysis, we consider three such network configurations, each operating under two progressively more sensitive instrument settings. The first setting, the A+ configuration (L. Barsotti et al. 2018), increases the accessible volume by a factor of ~ 8 relative to LIGO’s recently completed fourth observing run (O4); this is equivalent to an improvement in strain sensitivity by a factor of ~ 2 . The second, and the more ambitious A# (pronounced A-sharp) configuration (K. Kuns & P. Fritschel 2023), is expected to extend the detection volume by a factor of ~ 60 beyond O4.

We study the following network combinations in our analysis:

HLV+: which consists LIGO Hanford (H), LIGO Livingston (L), and Virgo (V) operating at A+ sensitivity;

HLI+: which uses LIGO Hanford, LIGO Livingston, and LIGO-India (I) at A+ sensitivity; and

HLI#: which also utilizes LIGO Hanford, LIGO Livingston, and LIGO-India, but at A[#] sensitivity.

2.3. Validation of the EM Follow-up Strategy

We analyze the validity of the proposed follow-up strategy, while considering three aspects of the problem.

(1) Expected detection rate of golden and silver dark sirens: We investigate the number of well-localized (0.1 deg², golden) and moderately localized (1 deg², silver) dark sirens that are expected within one year of observations under the A+ and A[#] detector sensitivities. No golden dark sirens are predicted to be identified with the HLV+ or HLI+ networks, but 4 potential golden candidates per year are expected with the A[#] sensitivity of HLI#. In contrast, several silver dark sirens will be detectable per year with both HLV+ and HLI+, and these become commonplace with HLI#.

(2) Suitability of HETDEX-style surveys for follow-up dark siren signals: We assess whether the VIRUS instrument on the HET is suitable for building event-specific catalogs in terms of completeness and redshift precision. We show that HETDEX-style VIRUS observations will provide precise spectroscopic redshifts and detect all galaxies with $M_g \sim -17.6$ out to $z \approx 0.2$. This sensitivity covers the redshift range of interest for near-future dark siren detections.

(3) Expected precision on the Hubble constant (H_0) from one year of observations: We show that for sources at $z \leq 0.2$, the error on H_0 inferred from the combination of ~ 25 golden and silver dark sirens under HLI# can potentially be within a few percent.

Together, these results demonstrate the feasibility and robustness of the proposed strategy. The improved sensitivity curves for LIGO, in conjunction with the depth and redshift resolution achieved by HETDEX-style surveys, provide the key to precision cosmology with gravitational waves.

3. STATISTICAL FRAMEWORK

In this Section, we outline the statistical formalism used to infer the Hubble constant from a population of dark sirens with spectroscopic galaxy follow-up. We first introduce the Bayesian framework for constructing the posterior on H_0 given the GW measurements and the associated galaxy redshift catalog. We then describe how selection effects and host-galaxy weighting enter the likelihood.

3.1. Bayesian Inference

Our analysis uses the Bayesian statistical framework. Let $\{x^{(i)}\}$, $i = 1 \dots N_{\text{GW}}$, denote the individual GW dark siren events, and for each event i , let $\{z_j^{(i)}\}$, $j = 1, \dots, N^{(i)}$ be the spectroscopic redshifts of the $N^{(i)}$ galaxies within the 90% sky area of the GW event. If $\{M_j^{(i)}\}$ are the absolute magnitudes of galaxies in the passband of interest, then the posterior distribution of H_0 is given by:

$$p\left(H_0 \mid \{x^{(i)}\}, \{z_j^{(i)}, M_j^{(i)}\}\right) \propto \mathcal{L}\left(\{x^{(i)}\} \mid H_0, \{z_j^{(i)}, M_j^{(i)}\}\right) \times \pi(H_0), \quad (1)$$

where \mathcal{L} denotes the joint likelihood of the GW data for the set of dark sirens $\{x^{(i)}\}$, given the cosmological model and the redshift measurement. Meanwhile, $\pi(H_0)$ is the prior on the Hubble constant, which is taken to be uniform in the interval $[60, 80] \text{ km s}^{-1} \text{ Mpc}^{-1}$.

In this work, we adopt two key assumptions that allow a clear statistical formulation of the dark-siren likelihood. First, we assume that the sample of galaxy redshifts is magnitude-complete within the GW localization volume, and reaches deep enough so that all galaxies that could plausibly host the event are included in the dataset. This is ensured for the mock data challenge that all true hosts have $M_g < -17.6$, which is the faintest absolute magnitude that can be detected at $z = 0.2$. Second, we treat the spectroscopic redshifts as unbiased and effectively exact for our purpose. The validity of these assumptions for HETDEX-like VIRUS observations are further discussed in Sec. 4.2.

Under these assumptions, the joint likelihood factorizes naturally over events, and for each event the contribution to the likelihood is obtained by marginalizing over all galaxies that could host the source:

$$\mathcal{L}(\{x^{(i)}\} \mid H_0, \{z_j^{(i)}, M_j^{(i)}\}) \propto \prod_i^{N_{\text{GW}}} \sum_j^{N^{(i)}} \frac{\mathcal{L}^{(i)}(x^{(i)} \mid \Omega_j^{(i)}, d_L(z_j^{(i)}, H_0))}{\beta(H_0)} p_{\text{Host}}(M_j^{(i)} \mid H_0). \quad (2)$$

Here $\{\Omega_j^{(i)}\}$, $j = 1, \dots, N^{(i)}$, are the sky positions of the $N^{(i)}$ galaxies within the 90% credible region of the i^{th} GW event, and the luminosity distance $d_L(z_j^{(i)}, H_0)$ connects the EM-observed redshift to the GW-inferred distance through the Hubble constant H_0 . The term p_{Host} encodes any desired luminosity weighting of host-galaxy probabilities, while the normalization term $\beta(H_0)$ captures GW selection effects—primarily detection efficiency—which are crucial for a self-consistent inference of H_0 .

There are two choices for the weighting in our analysis: no weighting, where every galaxy has the same likelihood of being the GW host, and linear weighting, where the host probability is proportional to its absolute luminosity (R. Gray 2021), i.e.,

$$p_{\text{Host}}(j) = \frac{L_j}{\sum_i^{N_{\text{gal}}} L_i}. \quad (3)$$

For our main results we adopt the no-weighting scheme, since our mock universe is not generated using a luminosity-weighted selection and applying such weights would therefore be inconsistent with the simulation model.

3.2. Selection Effects

A well-known selection effect in gravitational-wave astronomy is the analogue of the classical Malmquist bias, discussed in detail in B. F. Schutz (2011). In GW astronomy, Malmquist-like bias encompasses all selection effects that make certain types of binaries easier to detect than others. Because GW detectors are amplitude-limited, systems that produce intrinsically stronger strain waveforms are overrepresented in the detected population. This includes biases due to the distance–inclination degeneracy as face-on (or face-off) binaries appear brighter than edge-on ones at the same distance; mass distribution as heavier binaries have larger horizon distances; spin-induced precession and higher harmonics as binaries with significant in-plane spins or large mass ratios generate richer waveform structure and can be detected at greater distances; sky location relative to the detector network, which modulates the effective antenna response, and lastly astrophysical merger-rate evolution, which changes the relative number of detectable sources at different redshifts. All of these effects change the shape of the detected population, and all of them should be included in the full selection function $\beta(H_0)$. A rigorous numerical computation for the selection effects can be done in the most recent version of `gwcosmo` (S. Mastrogiovanni et al. 2023).

The form of the GW selection effects for golden and silver dark sirens follows the framework set by H.-Y. Chen et al. (2018) and M. Fishbach et al. (2019), with the assumption that the catalog of galaxy redshifts is magnitude complete with no other biases:

$$\beta(H_0) = \sum_j^{N_{\text{gal}}} P_{\text{det}}^{\text{GW}}(\Omega_j, d_L(z_j, H_0)) p_{\text{Host}}(j | \{z_j, M_j\}, H_0) \quad (4)$$

where

$$\begin{aligned} P_{\text{det}}^{\text{GW}}(\Omega_j, d_L(z_j, H_0)) = \\ \mathcal{L}(\text{SNR} > 12, \Delta\Omega_{90} < \Delta\Omega_{\text{threshold}} | \Omega_j, d_L(z_j, H_0)). \end{aligned} \quad (5)$$

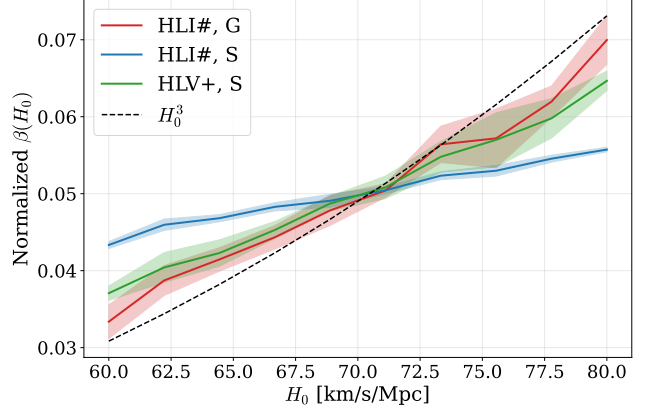


Figure 1. Numerically computed selection function for HLI# and HLV+, where G represents golden dark sirens with $\Delta\Omega_{90} \leq 0.1 \text{ deg}^2$ and S represents silver dark sirens with $\Delta\Omega_{90} \leq 1 \text{ deg}^2$.

where SNR is the signal-to-noise of the detection, and $\Delta\Omega_{\text{threshold}} = 0.1 \text{ deg}^2$ for golden dark sirens, and 1 deg^2 for silver dark sirens.

Figure 1 shows the numerically computed selection functions for golden and silver dark sirens for the HLI# and HLV+ detector networks. The selection function $\beta(H_0)$ is computed numerically using a Monte Carlo procedure based on simulated gravitational-wave injections generated with `GWBENCH`. For each injection, we record the network SNR and $\Delta\Omega_{90}$, and classify the event as detected if it satisfies $\text{SNR} > 12$ and a localization threshold corresponding for golden ($\Delta\Omega_{90} \leq 0.1 \text{ deg}^2$) to silver ($\Delta\Omega_{90} \leq 1 \text{ deg}^2$) dark sirens. The maximum redshift is taken as 0.2 to remain consistent with the rest of the work. To obtain a smooth estimate of the detection probability as a function of sky location and luminosity distance, we construct three-dimensional kernel density estimators (KDEs) in (α, δ, d_L) space for both the full injection set and the detected subset, using identical kernels and bandwidths. The GW detection probability $P_{\text{det}}^{\text{GW}}(\Omega, d_L)$ is then evaluated as the ratio of the detected to total KDEs, which captures the relative detection efficiency as a function of geometry and distance. For each value of H_0 , Monte Carlo samples are drawn uniformly over sky position and uniformly in comoving volume. The procedure is repeated with different random seeds to estimate the Monte Carlo uncertainty. Finally, the resulting selection functions are normalized such that $\int \beta(H_0) dH_0 = 1$, enabling direct comparison between detector networks and with the local-universe approximation, $\beta(H_0) \propto H_0^3$.

We find that the selection functions for HLI# golden and HLV+ silver dark sirens closely follow the local-universe $\beta(H_0) \propto H_0^3$ scaling; this is consistent with the

samples being dominated by nearby, high-SNR events. In contrast, the selection function for silver dark sirens detected with HLI# exhibits a more pronounced deviation from the H_0^3 approximation, reflecting the increasing importance of distance-dependent selection effects. No golden dark sirens are found for the HLV+ configuration, as discussed in Section 5 and hence the selection function for HLV+ golden dark sirens is not evaluated.

4. METHODS AND DATA

To test the robustness of the statistical framework, we first identify the golden and silver dark sirens from all events detectable in a year under each network, using the population model described below. A full Bayesian parameter estimation is performed for each of these golden and silver events. The distribution of galaxies is extracted from the fifth internal release of HETDEX.

4.1. GW Population Modeling and Inference

Our population analysis is carried out with **GWBENCH**, a fast Fisher-information-based forecasting tool designed to benchmark the performance of GW detector networks (S. Borhanian 2021). **GWBENCH** provides rapid estimates of sky localization, distance uncertainties, and parameter-estimation accuracy for compact-binary signals without requiring full Bayesian inference, making it well suited for population-level studies and survey design. For the purposes of this work, it enables us to efficiently model the detection and localization capabilities of future GW networks and to propagate these effects into predictions for dark-siren cosmology.

For this analysis we assume that the mass distribution of binary black holes (BBHs) follows the **POWER LAW + PEAK** model examined in the third Gravitational-Wave Transient Catalog[†] GWTC-3.0 (B. P. Abbott et al. 2019; R. Abbott et al. 2023), where the primary mass m_1 follows a power law with slope $\alpha = -3.4$ between $m_{\min} = 5 M_{\odot}$ and $m_{\max} = 87 M_{\odot}$, and smoothly tapers down below the minimum by a window width $\delta_m = 4.8 M_{\odot}$. A Gaussian component centered at $\mu_{\text{peak}} = 34 M_{\odot}$ with width $\sigma_{\text{peak}} = 3.6 M_{\odot}$ and fractional weight $\lambda = 0.04$ accounts for the excess of events near the pair-instability gap. The secondary mass is drawn via

$$p(q) \propto q^{\beta},$$

[†] Although the most recent GWTC-4.0 catalog (A. G. Abac et al. 2025) provides updated models for the mass distributions of black holes, this work was already well advanced when those results became available and a full reanalysis was not feasible. However, the revisions to the mass distribution are modest and do not materially affect our forecasts or alter any of our conclusions. For example, the local merger rate used in this work still lies within the newly predicted range.

with $\beta = 1.1$, where $q = m_2/m_1 < 1$ denotes the mass ratio.

The spin magnitudes of the black holes, which are restricted to align with the orbital angular momentum, follow a beta distribution (D. Wysocki et al. 2019):

$$p(\chi_i | \alpha_{\chi_i}, \beta_{\chi_i}) = \frac{\chi_i^{\alpha_{\chi_i}-1} (\chi_{\max} - \chi_i)^{\beta_{\chi_i}-1}}{B(\alpha_{\chi_i}, \beta_{\chi_i}) \chi_{\max}^{\alpha_{\chi_i} + \beta_{\chi_i} - 1}}, \quad (6)$$

where χ_i is the spin magnitude between $[0, \chi_{\max} = 1]$, and $B(\alpha_{\chi_i}, \beta_{\chi_i})$ is the beta function. This restriction excludes precession effects while modeling spins aligned with the orbital angular momentum.

The simulated population contains 10^6 BBH mergers distributed uniformly across five redshift bins spanning $0.005 \leq z \leq 3$, ensuring sufficient sampling across the detection range. The population is reweighted to follow a realistic redshift distribution modeled by the P. Madau & M. Dickinson (2014) star-formation-rate history,

$$\psi(z) = (1+z)^{\gamma} \left[1 + \left(\frac{1+z}{1+z_p} \right)^{\kappa} \right]^{-1}, \quad (7)$$

with $(z_p, \gamma, \kappa) = (1.9, 2.7, 5.6)$ (P. Madau 1997). This functional form is used here directly as a phenomenological parametrization of the redshift evolution of the BBH merger-rate density. In this approach, the effects of formation-to-merger time delays are incorporated implicitly through the assumed redshift dependence. We normalize the above equation to ensure that the simulated detections reflect realistic source populations with a local merger rate density consistent with $23.9_{-8.6}^{+14.3} \text{ Gpc}^{-3} \text{ yr}^{-1}$ (R. Abbott et al. 2021).

For the subset of events identified by **GWBENCH** as golden or silver dark sirens, we then transition from Fisher-matrix forecasts to a full Bayesian parameter-estimation analysis. Such an analysis is essential because GW events often exhibit non-Gaussian posteriors, higher-mode contributions, and distance-inclination degeneracies that cannot be reliably captured by Fisher approximations. By using a full Bayesian follow-up, we ensure that the key sources driving our H_0 sensitivity are treated with the highest-fidelity inference available.

The parameter estimation for the simulated golden and silver dark sirens is performed using the **bilby** Bayesian inference software (G. Ashton et al. 2019). We employ the *relative binning* technique—a fast, accurate method for evaluating GW likelihoods without requiring full waveform recomputation (K. Krishna et al. 2023; N. J. Cornish 2010; B. Zackay et al. 2018)—together with the **IMRPhenomXHM** waveform model (C. García-Quirós et al. 2020). This waveform family is particularly well suited to our analysis because it includes higher-order multipoles and models their influence consistently

across the inspiral, merger, and ringdown, which is essential for accurately constraining the inclination and luminosity distance of these events.

4.2. The HETDEX HDR5 data

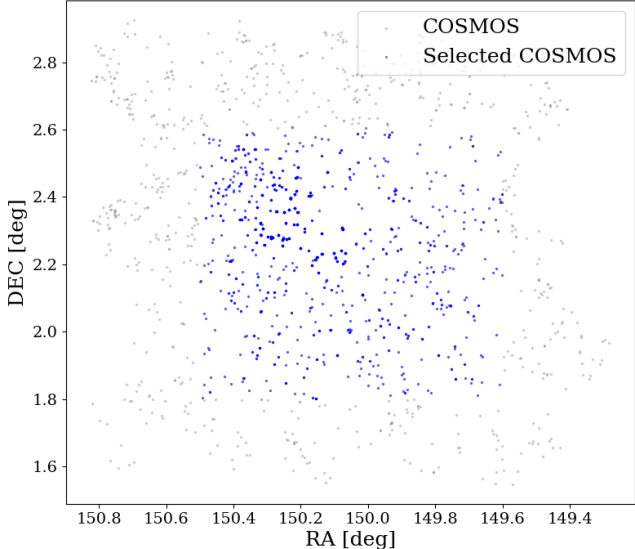


Figure 2. The distribution of galaxies in the COSMOS field. The blue points display those galaxies in the area selected for our mock data challenge with $z \leq 0.2$ and apparent magnitude $g \leq 22$. In the region shown, the HETDEX fill-factor is close to unity.

We draw our mock galaxies from the fifth internal data release of HETDEX. HETDEX is an untargeted spectroscopic survey designed to map the large-scale structure of Ly α -emitting galaxies between $1.9 < z < 3.5$, and thereby place a constraint on the evolution of Dark Energy (K. Gebhardt et al. 2021). To achieve this goal, the experiment uses the upgraded HET and VIRUS (G. J. Hill et al. 2021), a set of 78 IFU spectrographs, each delivering $R \sim 800$ spectra over the wavelength range $350 \text{ nm} < \lambda < 550 \text{ nm}$. As each IFU covers $51'' \times 51''$, VIRUS fills $\sim 22\%$ of the HET’s 18’ diameter field-of-view, and records a spectrum for every object whose light falls onto its fibers. Among these objects are local galaxies with $z \leq 0.2$.

The HETDEX survey consists of VIRUS observations in two large fields, a high Galactic latitude northern “spring” field and an equatorial “fall” field, and several smaller regions. Because HETDEX was designed to measure the signal of baryonic acoustic oscillations at $z \sim 2.5$, its sky footprint is not ideal for our mock data challenge. Specifically, the distribution of VIRUS IFUs on the HET focal plane is non-contiguous, and their orientation on the sky depends both on declination and

whether a field was observed during its “east” or “west” track on the sky. As a result, over most of the program’s survey fields, the HETDEX footprint is irregular with a fill-factor, defined as the fraction of the survey’s geometric area that is actually covered by usable data, is slightly less than 22%. However, being a HETDEX science verification field, the COSMic Evolution Deep Survey (COSMOS) field (N. Scoville et al. 2007; C. M. Casey et al. 2023) was observed by the survey multiple times, and as a result, it has a near-uniform fill-factor. This is demonstrated by Figure 2, which displays the positions of all of the field’s HETDEX ‘galaxy’ detections with $g \leq 22$ and $z \leq 0.2$. The uniform spatial coverage, especially near the field center, is ideal for our dark siren tests. To avoid the irregular geometric shape on the edge and maximize the fill-factor, we have selected the central blue region labeled “Selected COSMOS” for the mock sky background.

There is one drawback to using COSMOS in our dark siren challenge: because the field is relatively small, the effects of local large-scale structure will introduce a bias into the results (see Section 5). Therefore, to assess the robustness of our calculations, we also use the Spitzer-HETDEX Exploratory Large-Area (SHELA) field (a 24 deg^2 subset of the fall field; C. Papovich et al. 2016) in our dark siren analysis. This region is shown in Figure 3. While SHELA has a far lower ($\sim 20\%$) fill-factor and a much more fragmented tiling pattern, its ~ 30 times larger area presents a useful complementary dataset.

4.2.1. GW Mock Data Analysis

For this study, we simulate GW events at specific sky locations and then identify those that qualify as potential golden or silver dark sirens (i.e., those with $\Delta\Omega_{90} < 0.1 \text{ deg}^2$ and $\Delta\Omega_{90} < 1 \text{ deg}^2$) via a full Bayesian parameter estimation using `bilby` (G. Ashton et al. 2019). To emulate a realistic galaxy environment for each simulated event, we shift the sky coordinates of simulated GW source so that it aligns with that of an $M_g < -17.6$ galaxy in the COSMOS or SHELA field, whose luminosity distance (computed assuming $H_0 = 70 \text{ km s}^{-1} \text{ Mpc}^{-1}$) is closest—typically within 0.5%—to that of the simulated merger. This procedure ensures that the spatial distribution of galaxies in the mock catalog is consistent with the true sky location of the simulated GW event and that the galaxy sample used in the H_0 inference is complete.

We select galaxies as potential hosts based on the credible sky volume of each GW injection, before passing the information in the catalog onto Eq. (2). A galaxy is selected as a potential host if it satisfies both of the following conditions: (1) its sky location falls within the

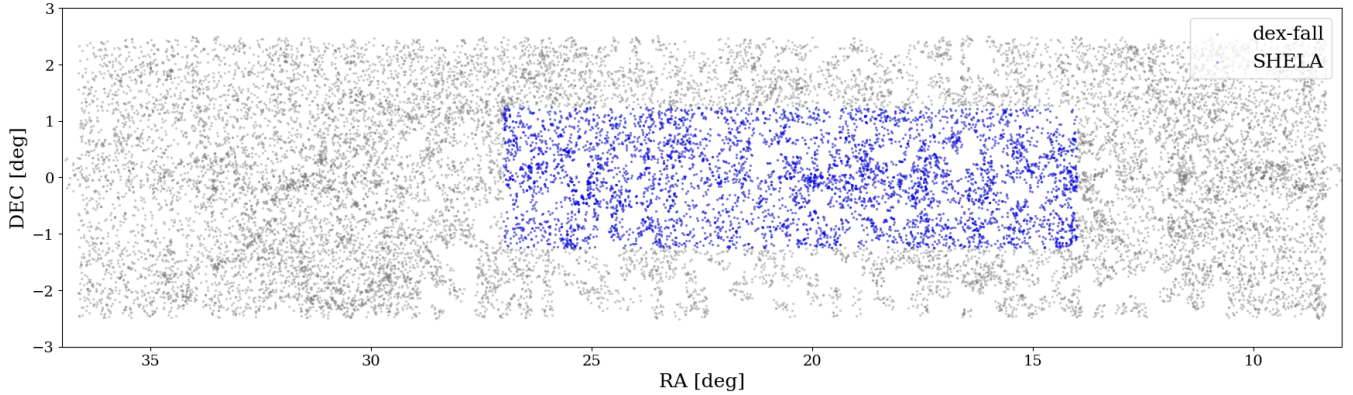


Figure 3. The distribution of galaxies in the HETDEX fall survey area. The blue points represent galaxies the SHELA field with $z \leq 0.2$ and apparent magnitude $g \leq 22$. The large void-like regions in the map are due to unobserved fields. SHELA provides a complementary data set to COSMOS in our mock data challenge: it is $\gtrsim 30$ larger area minimizes the effect of cosmic variance on our analysis, but its much lower fill-factor reduces the number of host galaxy candidates by a factor of ~ 4.6 .

90% credible region of the GW event and (2) its redshift is within the maximum redshift range corresponding to the 90% luminosity distance posterior, assuming a Hubble Constant in the range $[60, 80] \text{ km s}^{-1} \text{ Mpc}^{-1}$. We have verified that extending the sky area to encompass the 99% credible region leads to no noticeable change in the H_0 posterior.

4.2.2. Detection and Precision

HETDEX detects objects using two different analysis pipelines. The first, **ELiXer** (D. Davis et al. 2023), identifies and classifies all emission lines with fluxes greater than $\sim 5 \times 10^{-17} \text{ erg cm}^{-2} \text{ s}^{-1}$ (with the limit brightening to $\sim 40 \times 10^{-17} \text{ erg cm}^{-2} \text{ s}^{-1}$ in the extreme blue limit of the experiment’s spectral range). The second, **Diagnose**, operates on objects detected in the g -band continuum, which encompasses most of VIRUS’ spectroscopic bandpass. This pipeline classifies objects based on their absorption lines and assigns redshifts to sources as faint as $g \sim 23$ (G. R. Zeimann et al. 2024; E. Mentuch Cooper et al. 2023).

The HETDEX pipelines achieve redshift precisions ranging from $\sim 30 \text{ km s}^{-1}$ for bright, high signal-to-noise ratio sources to $\lesssim 100 \text{ km s}^{-1}$ for the faintest detections (K. Gebhardt et al. 2021; K. Hawkins et al. 2021). At the luminosity distances relevant for this work ($300 - 1000 \text{ Mpc}$), these uncertainties correspond to fractional redshift errors of 0.05%–0.15% in the best cases and 0.16%–0.50% for the worst cases (assuming $H_0 = 70 \text{ km s}^{-1} \text{ Mpc}^{-1}$). We therefore consider the effect of redshift uncertainty negligible for the purposes of constraining H_0 .

4.2.3. Depth and Completeness

HETDEX is designed primarily to detect and measure emission lines. Consequently, direct comparisons to

surveys which target objects based on their continuum brightness are difficult. For example, K. Gebhardt et al. (2021) have used artificial emission line experiments to characterize HETDEX completeness as a function of both emission-line flux and wavelength. However, there are few measurements in the literature of emission-line luminosity functions for comparison: the ones that exist either have much brighter flux limits, are severely compromised by sample size, pre-select targets on the basis of continuum brightness, or target the $\text{H}\alpha$ line, which is outside the HETDEX spectral range (see, e.g., J. J. Salzer et al. 2000; J. Gallego et al. 2002; R. Ciardullo et al. 2013). However, given that continuum analysis program **Diagnose** reports a confident classification for 98.5% of $g < 22$ detections, and 86.4% of detections with $g < 23$ (E. Mentuch Cooper et al. 2023), it would seem likely that for $g < 22$ objects, the HETDEX catalog is close to complete.

To confirm this assessment, we created a g -band luminosity function based on photometric magnitudes using the classic V/V_{max} method (M. Schmidt 1968; J. Huchra & W. L. W. Sargent 1973). For this calculation, we do not use the pseudo- g magnitudes derived from the HETDEX spectra; these data are often compromised by the combination of the limited field-of-view of each IFU and the non-contiguous distribution of IFUs across the HET’s focal plane. (This is especially true for extended objects which fall near an IFU edge.) Instead, we use the Source Extractor-based isophotal magnitudes (K. Barbary 2016) computed by **ELiXeR** (D. Davis et al. 2023) from the ancillary imaging surveys that HETDEX uses to assist in object classification; these data include g -band images from the Hyper Suprime-Cam Subaru Strategic Program (HSC-SSP; H. Aihara et al. 2022), the SHELA survey (G. C. K. Leung et al. 2023), and the Dark Energy Camera Legacy Survey (DECaLS A).

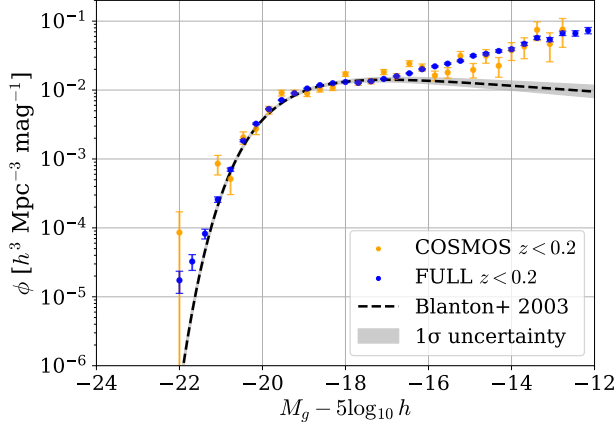


Figure 4. The g -band galaxy luminosity function derived from the HETDEX catalog compared to that found from the SDSS (M. R. Blanton et al. 2003). The orange points are derived solely from galaxies in the COSMOS field; the blue points represent galaxies from the full 79 deg^2 of the HETDEX DR5 catalog. The apparent magnitude limit is taken conservatively as $g \sim 22$. The steep increase in the number of galaxies fainter than $M_g \sim -17$ is also seen in the DESI DR2 data (S. G. Moore et al. 2025).

Dey et al. 2019), among others. (A full list of the images, along with their depths is given in Table 1 of D. Davis et al. 2023). These data go much deeper in the continuum than HETDEX spectroscopy, and do not require extrapolations for parts of galaxies that fall outside the $51'' \times 51''$ field of each VIRUS IFU. In all cases, when multiple images are available, we use the deepest data, and only where no ancillary images are available do we revert to the pseudo- g -band magnitudes computed from HETDEX spectra (as described in K. Gebhardt et al. 2021 and E. Mentuch Cooper et al. 2023).

Figure 4 compares the luminosity function derived from the HETDEX data to the fitted Schechter function (P. Schechter 1976) of SDSS ($\phi_* = 2.18 \pm 0.33$, $M_* - 5 \log_{10} h = -19.39 \pm 0.02$ and $\alpha = 0.89 \pm 0.03$; M. R. Blanton et al. 2003). For the figure, all the g -band magnitudes described above have been corrected for foreground extinction using the line-of-sight reddening estimates from the E. F. Schlafly & D. P. Finkbeiner (2011) recalibration of the D. J. Schlegel et al. (1998) dust maps, using a standard $R_V = 3.1$ extinction law. (In all cases, these corrections are quite small, as the HETDEX fields were originally selected to have minimal Galactic reddening.) To be consistent with M. R. Blanton et al. (2003), our absolute g -band magnitudes have been calculated using an averaged k-correction for each redshift bin obtained from the Galaxy And Mass Assembly data (GAMA; S. P. Driver et al. 2022), and a luminosity density evolution of $Q * (z - 0.1)$, where Q is taken to be 2.04. Overall, the agreement between the

two measurements is excellent for absolute magnitudes brighter than $M_g \sim -18$. At fainter magnitudes, the SDSS function is best fit by a flat power-law with a faint slope of $\alpha \sim -0.9$. Figure 4 displays this function, and its extrapolation beyond $M_g \sim -16$. In contrast, the HETDEX luminosity function increases steeply at magnitudes fainter than $M_g \sim -18$, with a slope closer to $\alpha \sim -1.4$. This behavior is in excellent agreement with that derived by S. G. Moore et al. (2025) for DESI-DR2 galaxies.

The luminosity function of Figure 4 and its agreement with that found by DESI-DR2 presents a strong argument for the completeness of HETDEX. Specifically, at $z \leq 0.1$, the HETDEX catalog represents a volume-limited dataset for all galaxies more luminous than $M_g \sim -15.4$, i.e., a full magnitude fainter than the Small Magellanic Cloud. Even at $z = 0.2$, this limit only brightens to $M_g \sim -17.6$, a value similar to the absolute magnitude of the Large Magellanic Cloud.

Finally, we can compare our results to those found by V. Alfradique et al. (2025) using the **Magneticum** suite of cosmological simulations. Using the simulation’s mock galaxy dataset, the authors quantified parent galaxy detection completeness as a function of r -band apparent magnitude and found that, within 1600 Mpc ($z = 0.307$ for $H_0 = 70 \text{ km s}^{-1} \text{ Mpc}^{-1}$), an apparent magnitude cut of $r \sim 22$ yields 98% completeness. This result is similar to what should be attained with VIRUS: although local galaxies can be up to a magnitude fainter in g than in r (e.g., E. F. Bell et al. 2003), our smaller redshift limit of $z < 0.2$ ($D_L \lesssim 980 \text{ Mpc}$) more than compensates for this systematic effect. Moreover, any residual incompleteness is further mitigated by weighting by galaxy properties: e.g., if host likelihood scales with star-formation rate, missing a few faint dwarf elliptical/spheroidal galaxies matters very little, while the emission-lines associated with star formation will increase VIRUS survey depth. In short, HETDEX style-observations with VIRUS achieve over 98% completeness in our distance range, so galaxy incompleteness should not significantly increase the H_0 error. We conclude that almost all potential galaxy hosts within $z = 0.2$ will be captured by a dedicated VIRUS survey by HET.

5. RESULTS

Figure 5 shows the **GWBENCH** predictions for the number of GW events expected per year as a function of their 90% credible sky area for the three detector network configurations under consideration. Table 1 summarizes this information by giving the expected number of dark siren events classified as either golden or silver.

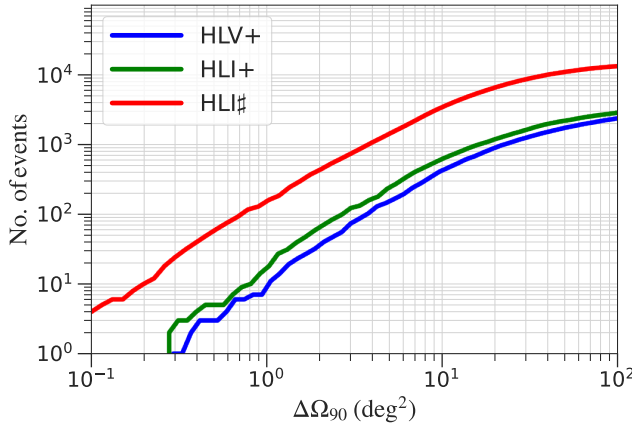


Figure 5. The expected number of GW events detected by the HLV+, HLI+, and HLI# networks as a function of their 90% credible sky area.

The results show a clear improvement in sky localization with each upgrade in the detector sensitivity. We also notice that the HLI+ network detects more well-localized events than HLV+ due to the longer baseline between LIGO-India and LIGO Hanford or Livingston. Events with a 90% credible sky area smaller than 1 deg^2 are detected in all of the networks considered, and the number of these silver events is much larger in the HLI# network. More importantly, events with localizations below $\Delta\Omega_{90} < 0.1 \text{ deg}^2$, i.e., the golden sirens, begin to appear in HLI#. These numbers provide a robust estimate on the approximate number of follow-up events that would be available for an HET-like program, provided that they occur in the northern hemisphere.

Our mock data analysis uses HETDEX data in the central 1 deg^2 region of the COSMOS field. In area, this matches the upper limit for the definition of our silver dark sirens. However, since GW sky localizations are frequently elongated with irregular geometries, a single event’s 90% region may extend beyond the limits of our data. To guarantee full coverage using our galaxy catalog, we tile the field by compactly replicating it along its edges, ensuring that the effective background area always exceeds the sky localization. The resulting pattern is shown in Figure 6. The figure also illustrates the positional uncertainty of a typical silver dark siren with

Network	$\Delta\Omega_{90} < 0.1 \text{ deg}^2$	$\Delta\Omega_{90} < 1 \text{ deg}^2$
HLV+	0	7
HLI+	0	17
HLI#	4	136

Table 1. Expected number of GW events per year with sky area under 0.1 deg^2 (typical golden dark sirens) and 1 deg^2 (typical silver dark sirens).

multiple possible host galaxies. This particular silver event uses the region of the COSMOS field where HETDEX has nearly 100% spectroscopic coverage. Consequently, the example represents a realistic expectation with future detector networks.

Figure 7 shows the corner plot and corresponding sky map for a representative golden dark siren in the SHELA field. In this example, a single galaxy (shown in purple) dominates the H_0 posterior. This event has relatively few potential hosts because the HETDEX HDR5 fill-factor of the region is relatively low (only $\sim 20\%$). Whether our observational criterion for identifying a “golden” dark siren (i.e., $\Delta\Omega_{90} \leq 0.1 \text{ deg}^2$) coincides with the definition commonly used in the literature (i.e., the presence of a single plausible host) depends sensitively on the galaxy density of the sky region in which the GW event occurs.

Figure 8 illustrates the H_0 posteriors resulting from each mock data challenge for the different GW networks, HETDEX catalogs and the number of years of GW observations. We did not apply any luminosity weighting in our analysis as our mock universe assumes no correlation between the probability of a galaxy hosting a CBC merger and its luminosity. However, for this study, we restricted the luminosity distance of simulated events to be smaller than 980 Mpc (i.e., $z \leq 0.2$ with $H_0 = 70 \text{ km s}^{-1} \text{ Mpc}^{-1}$) and the absolute magnitudes of the true hosts to be greater than $M_g = -17.6$. These choices ensure that our magnitude-completeness assumption remains valid. A brief summary of the results of our analysis is as follows:

- HLI# (silver + golden; 25 events; COSMOS field): $H_0 = 66.61_{-0.83}^{+1.26} (+1.9\%) \text{ km s}^{-1} \text{ Mpc}^{-1}$
- HLI# (golden only; 3 events; COSMOS field): $H_0 = 71.7_{-3.45}^{+7.43} (+10.4\%) \text{ km s}^{-1} \text{ Mpc}^{-1}$
- HLV+ (silver; 4 events; COSMOS field): $H_0 = 72.58_{-5.88}^{+5.22} (+7.2\%) \text{ km s}^{-1} \text{ Mpc}^{-1}$
- HLI# (silver + golden; 25 events; SHELA field): $H_0 = 69.18_{-0.62}^{+0.67} (+1.0\%) \text{ km s}^{-1} \text{ Mpc}^{-1}$.

Our results highlight both the strengths and limitations of mock data challenge. On the positive side, our approach shows that just a handful of golden and silver sirens are enough to place tight constraints on H_0 . For example, in the HLI# configuration, all it takes is 25 events to achieve a H_0 measurement that is good to a few-percent. However, the results also show that when we limit our mock data challenge to a single region of space – the COSMOS field – we become susceptible to biases from the field’s large-scale structure. In Figure 9,

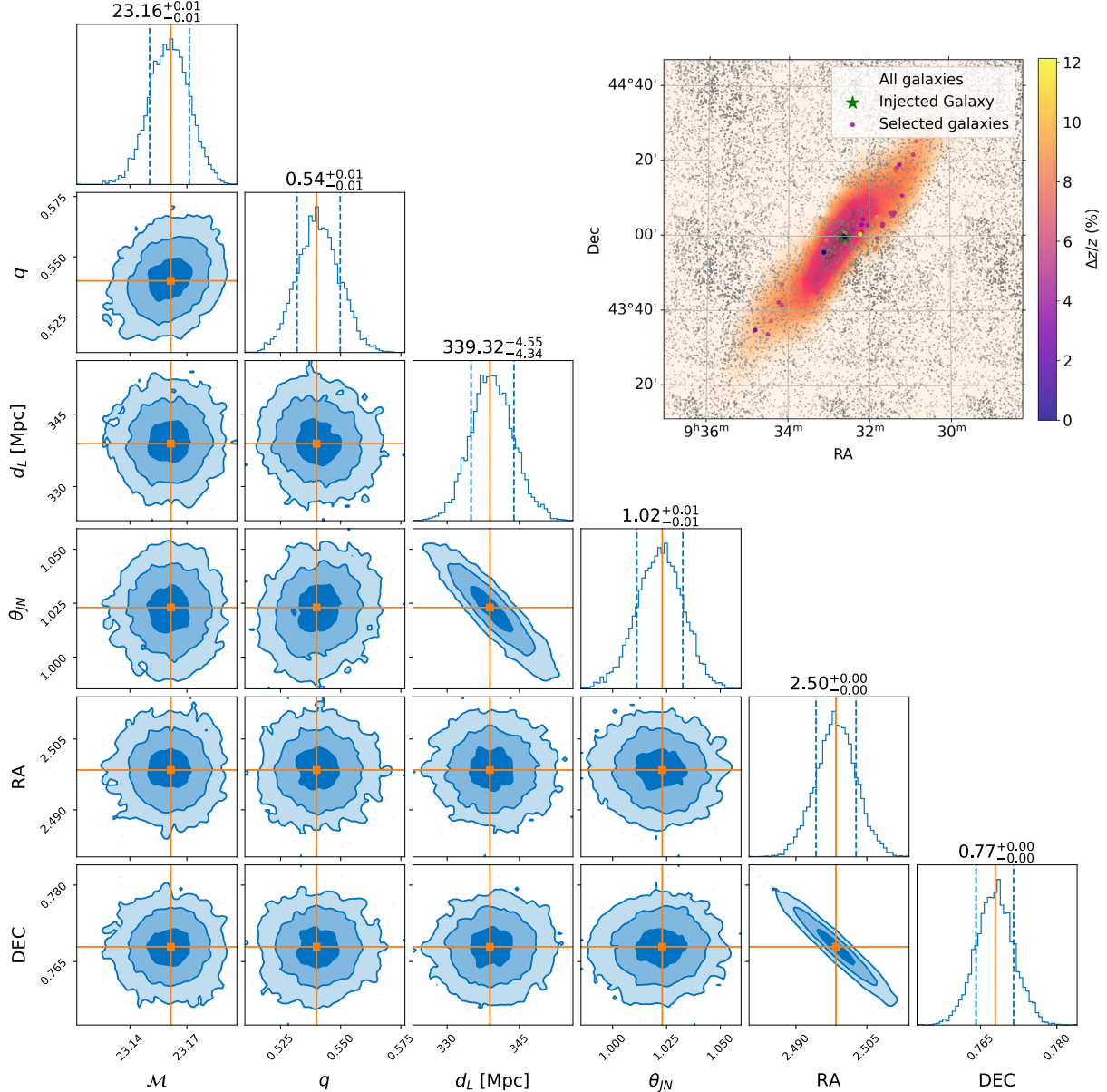


Figure 6. Example of a silver dark siren with $\Delta\Omega_{90} = 0.18 \text{ deg}^2$. The corner plot shows the `bilby` posteriors results of chirp mass (\mathcal{M}), mass ratio (q), luminosity distance (d_L), inclination (θ_{JN} as no precession is injected), Right Ascension (RA) and Declination (DEC). The sky map displays the 90% credible region, along with the galaxies of the COSMOS field. The green star represents the injected galaxy. Galaxies that are identified as potential hosts are displayed as circles; these are the systems that contribute to the H_0 posterior.

we illustrate this by showing 1-year, 2-year, and 3-year results based on the galaxies of COSMOS and SHELA. COSMOS contains a prominent galaxy overdensity at $z \sim 0.13$, and a less pronounced one at $z \sim 0.18$, violating the assumption of cosmological homogeneity. Because our simulated events span a range of redshifts, they are affected by the large number of possible hosts in these structures, leading to a bias that fluctuates as additional events are accumulated. In contrast, the larger

area of the SHELA field mitigates the systematic error introduced by cosmic variance, resulting in an unbiased inference that remains stable as the number of events increases. However due to its lower fill-factor, the uncertainty in H_0 derived from its analysis is significantly underestimated.

In a realistic scenario, each GW event will occur against a different galaxy field with a different redshift-distribution of potential host galaxies. Consequently,

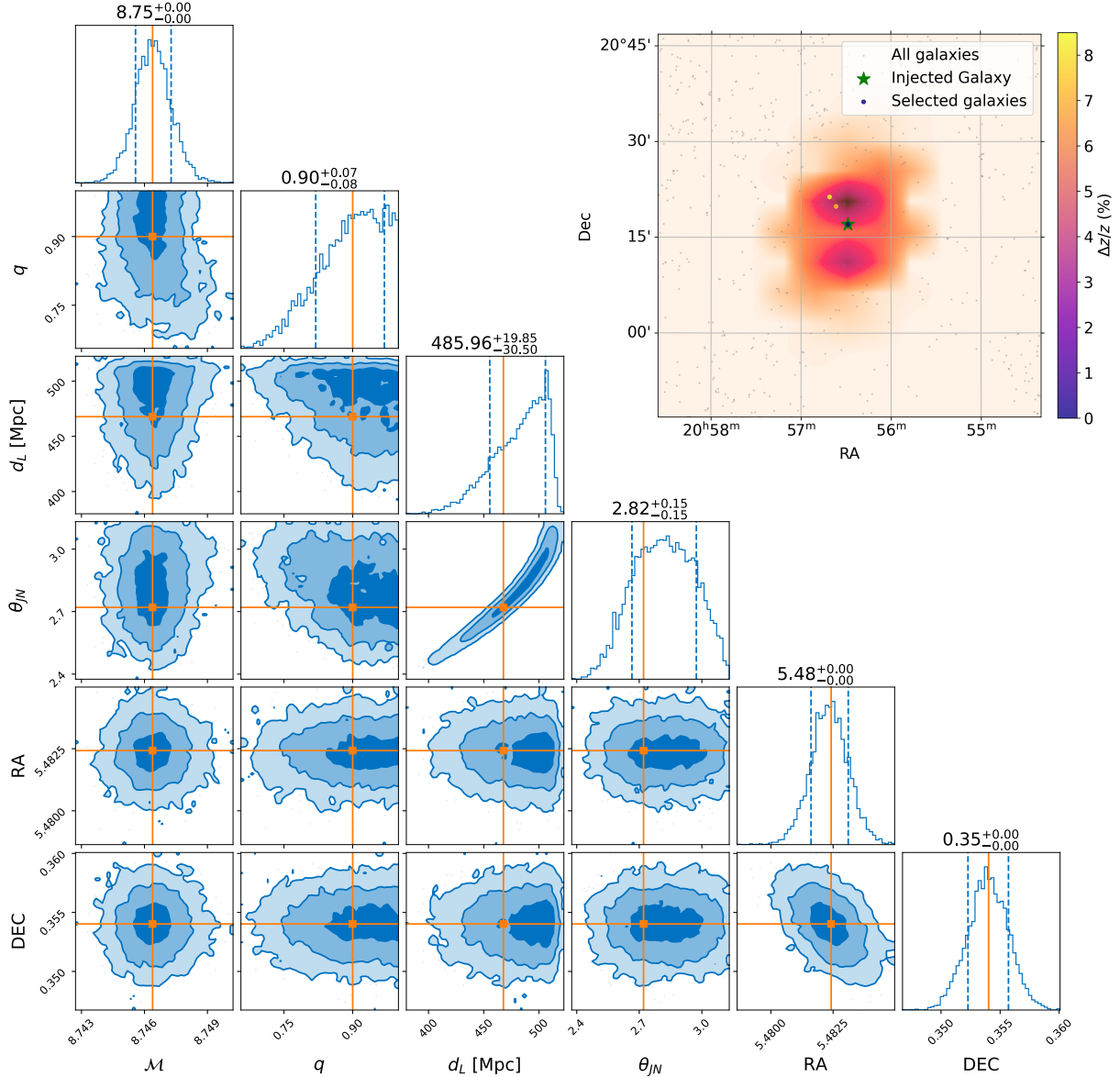


Figure 7. Example of a golden dark siren with $\Delta\Omega_{90} = 0.07 \text{ deg}^2$. The corner plot shows the `bilby` parameter estimation results for the same set of parameters described in Fig. 6; the sky map displays the 90% credible region, along with galaxies in the SHELDA field in HETDEX that have been filtered out as potential hosts. The green star represents the injected galaxy. Only one galaxy (in purple, coincident with the injected galaxy) dominates the H_0 posterior; the other candidates (in yellow) deviate substantially in luminosity distance.

while the posterior of any single GW event may be affected by a field's large-scale structure, the biases from an ensemble of events distributed over different fields will average out. This underscore the importance of accumulating golden and silver dark sirens across multiple, widely separated sky regions to help mitigate the effect of field-specific clustering biases.

Figure 10 illustrates the relationship between the 90% credible sky area ($\Delta\Omega_{90}$) and the number of galaxies enclosed within the corresponding credible volume for each event. In panel (a), we consider all galaxies within the

localization region. As expected, events with smaller sky localization areas contain significantly fewer candidate hosts. The COSMOS field is more densely populated than the SHELDA field, so the number of potential hosts is larger, despite having the same GW sky area. This feature also explains the narrower H_0 posterior obtained with SHELDA (see Fig. 8).

In our analysis, we begin with a flat prior that that every galaxy, regardless of luminosity, has the same likelihood of being the host of a GW event. Thus, as illustrated by the luminosity function of Figure 4, most of the

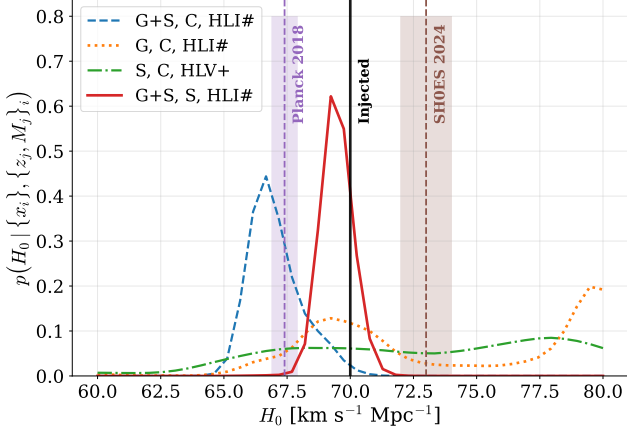


Figure 8. H_0 posterior obtained from the accumulation of a year’s worth of golden and silver dark siren follow-up observations with $z \leq 0.2$ under each future network. The first labels G+S, G, and S denote golden and silver dark sirens, only golden dark sirens, and only silver dark sirens respectively. The second labels C and S denote either COSMOS field or SHELA field as mock sky background. The last labels HLI#, HLV+ denote each network configuration.

galaxies contained in the 90% credible region are faint. If we were to restrict our analysis to $L > L^*$ galaxies, then the number of possible hosts would drop significantly. This is shown in panel (b) of Figure 10, which shows that the majority of events have fewer than 20 galaxy host candidates. This suggests that if luminosity weighting were to be used, golden and silver dark sirens with only one or several host candidates dominating the H_0 posterior would become much more common. The conversion to a percent level value for the H_0 would require far fewer events.

6. DISCUSSION AND CONCLUSIONS

The results presented in Section 5 demonstrate the significant improvement in sky localization and cosmological inference achievable with upgraded gravitational-wave detector networks operating at A+ and A[#] sensitivities. As summarized in Table 1, the transition from HLV+ to HLI# increases the number of well-localized dark sirens by more than an order of magnitude. In particular, the HLI# network produces several golden dark siren events ($\Delta\Omega_{90} < 0.1 \text{ deg}^2$), marking the first time such precision becomes feasible for binary black hole mergers.

The examples shown in Figs. 6 and 7 illustrate how improved detector sensitivity directly translates into tighter sky areas and reduced host-galaxy degeneracy. While golden dark sirens may still depend on the luck of not falling in a overdense region of sky, silver sirens should be common and provide a robust statistical path

toward an independent measurement of the Hubble constant.

Combining one year of simulated detections can potentially yield an H_0 precision at the percent level for the most sensitive network HLI#. However it should be noted that the HET can only access about 57% of the sky, and without an instrument equivalent to VIRUS in the southern hemisphere, it might require more years of observation to achieve the predicted precision. Overall, these findings confirm that with improved detector sensitivity and adequate galaxy surveys, dark sirens will eventually become a competitive and independent probe of the local expansion rate of the Universe.

Several limitations in our current analysis should be noted. First, we have not accounted for the contribution of peculiar velocities to the observed redshift, which can introduce an additional uncertainty of $\sim 1\text{--}2\%$ in H_0 for nearby sources. This effect becomes important when the cosmological redshift is comparable to the typical peculiar-velocity dispersion. Second, the galaxy catalogs used in this work cover only small sky areas, making our measurements highly sensitive to the large-scale structure in the host field. A comparison of COSMOS and SHELA shows that field-specific clustering can introduce noticeable biases that grow with increasing numbers of events. In COSMOS, the limited field size causes introduces a systematic in the H_0 posterior that reflects the region’s large-scale structure; in SHELA, which is almost 30 times larger, the effect is much less pronounced, though the lower fill-factor artificially narrows the posterior. We expect that for real GW detections, which occur all over the sky, the effects of field-specific clustering will be minimal. However, for mock studies such as that performed here, the effect can dominate the results. Both issues related to the galaxy catalog can be addressed easily: (a) perform efficient **galaxy clustering** so the marginalization is carried out over *independent host environments* rather than over many correlated galaxies in the same large-scale structure, and (b) ensure follow-up catalogs have **fill factors near unity**, so host-galaxy incompleteness does not introduce field-dependent selection biases.

ACKNOWLEDGMENTS

The authors wish to thank Archisman Ghosh for a careful reading of the manuscript and invaluable comments that helped improve the presentation. Y.D. thanks Yi Qiu, Alberto Salvarese, Giovanni Benetti, Kuan Wang, Koustav Chandra and Olivia Curtis for helpful discussions. Y.D. is partially supported by NSF grant AST-2307147 and B.S.S. acknowledges support from National Science Foundation (NSF) grants

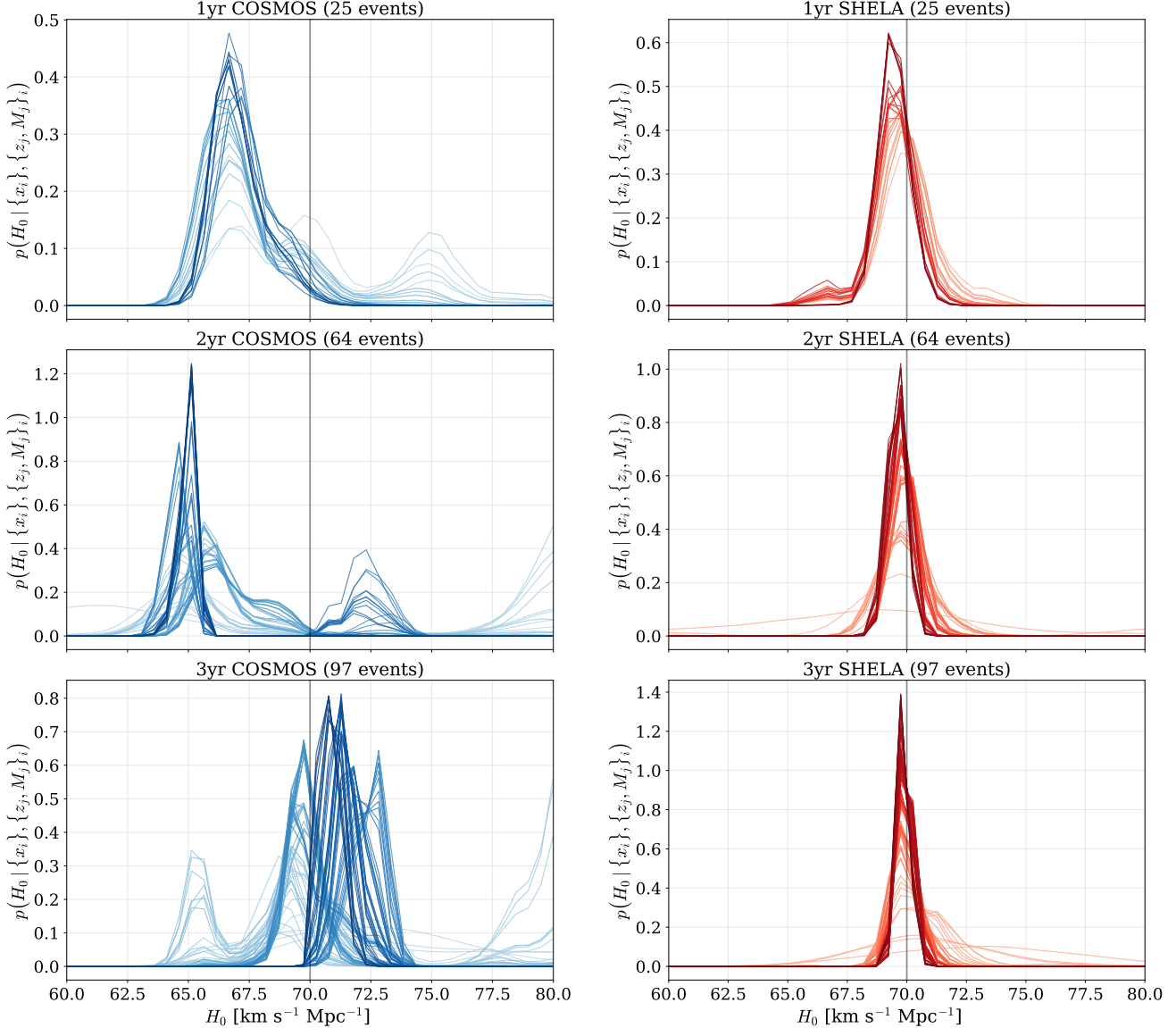


Figure 9. Evolution of the H_0 posterior obtained from one, two, and three years of golden and silver dark sirens within $z = 0.2$, using the COSMOS (Left) or SHELA (Right) field as the mock sky background under the HLI# network. The color progressively darkens as additional events are added to the catalog. The injected value is $H_0 = 70 \text{ km s}^{-1} \text{ Mpc}^{-1}$, and no luminosity weighting is applied.

AST-2307147, PHY-2308886 and PHY-2309064. I.G. acknowledges support from the Network for Neutrinos, Nuclear Astrophysics, and Symmetries (N3AS) Collaboration, NSF grant: PHY-2020275. R.C. and C.G. acknowledges support from the NSF under grant AST-2408358. H.Y.C. is supported by the NSF under Grant PHY-2308752. R.G. is supported by STFC grant ST/V005634/1. D.J. was supported by the NSF under Grant AST-2307026. S.S. acknowledges support from the National Science Foundation under grants NSF-2219212 and NSF-2511145. The authors would also like to acknowledge the LIGO Laboratory

computing resources supported by NSF grants:PHY-0757058 and PHY-0823459, and the Gwave cluster maintained by the Institute for Computational and Data Sciences at Penn State University, supported by NSF grants: OAC2346596, OAC2201445, OAC2103662, OAC2018299, and PHY-2110594. The Institute for Gravitation and the Cosmos is supported by the Eberly College of Science and the Office of the Senior Vice President for Research at the Pennsylvania State University.

HETDEX is led by the University of Texas at Austin McDonald Observatory and Department of Astronomy with participation from the Ludwig-Maximilians-

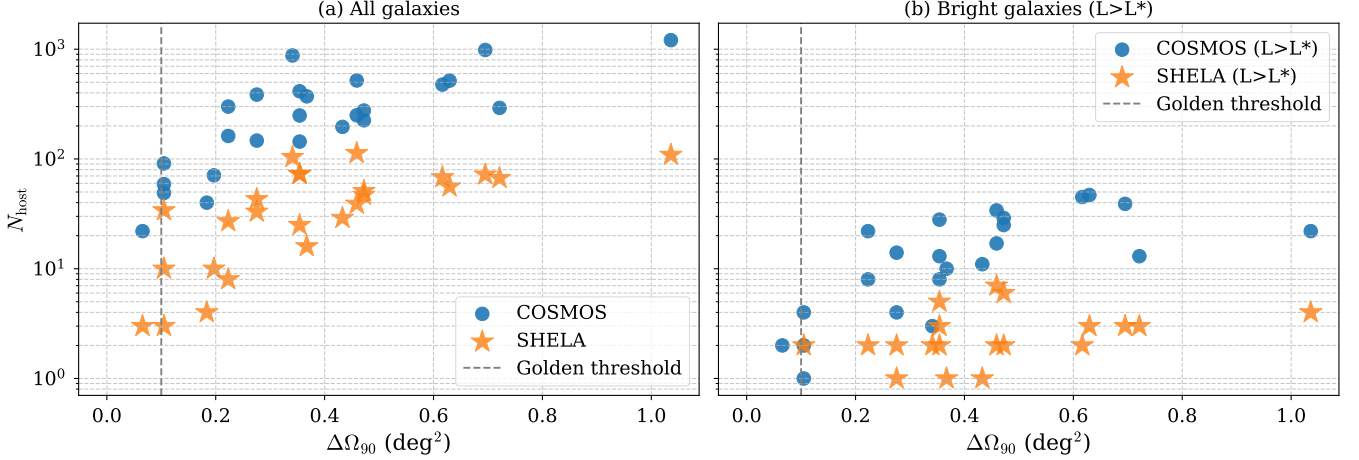


Figure 10. (a) Number of galaxies contained within the 90% credible sky areas ($\Delta\Omega_{90}$) for each GW injection. (b) Same as panel (a), but showing only galaxies with luminosities exceeding the characteristic luminosity L^* . Blue dots represent simulations using the COSMOS field as the background galaxy catalog, while orange stars represent those using the SHELA field. The vertical dashed line marks the “golden” threshold at $\Delta\Omega_{90} = 0.1 \text{ deg}^2$. The SHELA field, being less complete, typically yields fewer host candidates per event because of its sparser sampling and lower source density.

Universität München, Max-Planck-Institut für Extraterrestrische Physik (MPE), Leibniz-Institut für Astrophysik Potsdam (AIP), Texas A&M University, Pennsylvania State University, Institut für Astrophysik Göttingen, The University of Oxford, Max-Planck-Institut für Astrophysik (MPA), The University of Tokyo and Missouri University of Science and Technology.

Observations for HETDEX were obtained with the Hobby-Eberly Telescope (HET), which is a joint project of the University of Texas at Austin, the Pennsylvania State University, Ludwig-Maximilians-Universität München, and Georg-August-Universität Göttingen. The HET is named in honor of its principal benefactors, William P. Hobby and Robert E. Eberly. The Visible Integral-field Replicable Unit Spectrograph (VIRUS) was used for HETDEX observations. VIRUS is a joint project of the University of Texas at Austin, Leibniz-Institut für Astrophysik Potsdam (AIP), Texas A&M University, Max-Planck-Institut für Extraterrestrische Physik (MPE), Ludwig-Maximilians-Universität München, Pennsylvania State University, Institut für Astrophysik Göttingen, University of Oxford, and the Max-Planck-Institut für Astrophysik (MPA).

The authors acknowledge the Texas Advanced Computing Center (TACC) at The University of Texas at

Austin for providing high performance computing, visualization, and storage resources that have contributed to the research results reported within this paper. URL: <http://www.tacc.utexas.edu>

Funding for HETDEX has been provided by the partner institutions, the National Science Foundation, the State of Texas, the US Air Force, and by generous support from private individuals and foundations.

GAMA is a joint European-Australasian project based around a spectroscopic campaign using the Anglo-Australian Telescope. The GAMA input catalogue is based on data taken from the Sloan Digital Sky Survey and the UKIRT Infrared Deep Sky Survey. Complementary imaging of the GAMA regions was obtained by a number of independent survey programmes including GALEX MIS, VST KiDS, VISTA VIKING, WISE, Herschel-ATLAS, GMRT and ASKAP providing UV to radio coverage. GAMA is funded by the STFC (UK), the ARC (Australia), the AAO, and the participating institutions. The GAMA website is <https://www.gama-survey.org/>

Software: `astropy` (A. M. Price-Whelan et al. 2018), `GWENCH` (S. Borhanian 2021), `bilby` (G. Ashton et al. 2019), `Matplotlib` (J. D. Hunter 2007), `NumPy` (C. R. Harris et al. 2020), `SciPy` (P. Virtanen et al. 2020), `EliXer` (D. Davis et al. 2023).

REFERENCES

Abac, A. G., et al. 2025, <https://arxiv.org/abs/2508.18083>

Abbott, B. P., Abbott, R., Abbott, T. D., et al. 2017a,

Nature, 551, 85, doi: [10.1038/nature24471](https://doi.org/10.1038/nature24471)

Abbott, B. P., Abbott, R., Abbott, T. D., et al. 2017b,

ApJL, 848, L12, doi: [10.3847/2041-8213/aa91c9](https://doi.org/10.3847/2041-8213/aa91c9)

Abbott, B. P., et al. 2019, *ApJL*, 882, L24, doi: [10.3847/2041-8213/ab3800](https://doi.org/10.3847/2041-8213/ab3800)

Abbott, R., et al. 2021, *ApJL*, 913, L7, doi: [10.3847/2041-8213/abe949](https://doi.org/10.3847/2041-8213/abe949)

Abbott, R., et al. 2023, *Phys. Rev. X*, 13, 011048, doi: [10.1103/PhysRevX.13.011048](https://doi.org/10.1103/PhysRevX.13.011048)

Afroz, S., & Mukherjee, S. 2024, *Mon. Not. Roy. Astron. Soc.*, 534, 1283, doi: [10.1093/mnras/stae2139](https://doi.org/10.1093/mnras/stae2139)

Aghanim, N., et al. 2020, *A&A*, 641, A6, doi: [10.1051/0004-6361/201833910](https://doi.org/10.1051/0004-6361/201833910)

Aihara, H., AlSayyad, Y., Ando, M., et al. 2022, *PASJ*, 74, 247, doi: [10.1093/pasj/psab122](https://doi.org/10.1093/pasj/psab122)

Alfradique, V., Bom, C. R., & Castro, T. 2025, *PhRvD*, 112, 063561, doi: [10.1103/vd36-3mys](https://doi.org/10.1103/vd36-3mys)

Ashton, G., et al. 2019, *ApJS*, 241, 27, doi: [10.3847/1538-4365/ab06fc](https://doi.org/10.3847/1538-4365/ab06fc)

Bailes, M., et al. 2021, *Nature Rev. Phys.*, 3, 344, doi: [10.1038/s42254-021-00303-8](https://doi.org/10.1038/s42254-021-00303-8)

Barbary, K. 2016, *The Journal of Open Source Software*, 1, 58, doi: [10.21105/joss.00058](https://doi.org/10.21105/joss.00058)

Barsotti, L., Fritschel, P., Evans, M., & Gras, S. 2018, Updated Advanced LIGO sensitivity design curve, Technical Notes, LIGO-T1800044,, <https://dcc.ligo.org/LIGO-T1800044/public>

Barsotti, L., Fritschel, P., Evans, M., & Gras, S. 2018, Updated Advanced LIGO sensitivity design curve, Technical Notes, LIGO-T1800044,, <https://dcc.ligo.org/LIGO-T1800044/public>

Bell, E. F., McIntosh, D. H., Katz, N., & Weinberg, M. D. 2003, *ApJS*, 149, 289, doi: [10.1086/378847](https://doi.org/10.1086/378847)

Bera, S., Rana, D., More, S., & Bose, S. 2020, *ApJ*, 902, 79, doi: [10.3847/1538-4357/abb4e0](https://doi.org/10.3847/1538-4357/abb4e0)

Blanton, M. R., et al. 2003, *ApJ*, 592, 819, doi: [10.1086/375776](https://doi.org/10.1086/375776)

Borhanian, S. 2021, *Classical and Quantum Gravity*, 38, 175014, doi: [10.1088/1361-6382/ac1618](https://doi.org/10.1088/1361-6382/ac1618)

Borhanian, S., Dhani, A., Gupta, A., Arun, K. G., & Sathyaprakash, B. S. 2020, *ApJL*, 905, L28, doi: [10.3847/2041-8213/abcaf5](https://doi.org/10.3847/2041-8213/abcaf5)

Branchesi, M., et al. 2023, *JCAP*, 07, 068, doi: [10.1088/1475-7516/2023/07/068](https://doi.org/10.1088/1475-7516/2023/07/068)

Casey, C. M., et al. 2023, *ApJ*, 954, 31, doi: [10.3847/1538-4357/acc2bc](https://doi.org/10.3847/1538-4357/acc2bc)

Chen, A. 2025, *JCAP*, 2025, 076, doi: [10.1088/1475-7516/2025/07/076](https://doi.org/10.1088/1475-7516/2025/07/076)

Chen, H.-Y., Fishbach, M., & Holz, D. E. 2018, *Nature*, 562, 545, doi: [10.1038/s41586-018-0606-0](https://doi.org/10.1038/s41586-018-0606-0)

Ciardullo, R., Gronwall, C., Adams, J. J., et al. 2013, *ApJ*, 769, 83, doi: [10.1088/0004-637X/769/1/83](https://doi.org/10.1088/0004-637X/769/1/83)

Collaboration, T. L. S., Aasi, J., Abbott, B. P., et al. 2015, *Class. Quant. Gravity*, 32, 074001, doi: [10.1088/0264-9381/32/7/074001](https://doi.org/10.1088/0264-9381/32/7/074001)

Cornish, N. J. 2010, <https://arxiv.org/abs/1007.4820>

Cousins, B., Schumacher, K., Chung, A. K.-W., et al. 2025, <https://arxiv.org/abs/2503.01997>

Cross-Parkin, M. L., Howlett, C., Davis, T. M., & Khetan, N. 2025, Dark sirens and the impact of redshift precision, *arXiv*, doi: [10.48550/arXiv.2502.17747](https://doi.org/10.48550/arXiv.2502.17747)

Dálya, G., Galgóczi, G., Dobos, L., et al. 2018, *Mon. Not. Roy. Astron. Soc.*, 479, 2374, doi: [10.1093/mnras/sty1703](https://doi.org/10.1093/mnras/sty1703)

Dálya, G., et al. 2022, *Mon. Not. Roy. Astron. Soc.*, 514, 1403, doi: [10.1093/mnras/stac1443](https://doi.org/10.1093/mnras/stac1443)

Davis, D., Gebhardt, K., Cooper, E. M., et al. 2023, *ApJ*, 946, 86, doi: [10.3847/1538-4357/acb0ca](https://doi.org/10.3847/1538-4357/acb0ca)

Dey, A., Schlegel, D. J., Lang, D., et al. 2019, *AJ*, 157, 168, doi: [10.3847/1538-3881/ab089d](https://doi.org/10.3847/1538-3881/ab089d)

Di Valentino, E., Melchiorri, A., & Silk, J. 2019, *Nature Astron.*, 4, 196, doi: [10.1038/s41550-019-0906-9](https://doi.org/10.1038/s41550-019-0906-9)

Di Valentino, E., Mena, O., Pan, S., et al. 2021, *Class. Quant. Grav.*, 38, 153001, doi: [10.1088/1361-6382/ac086d](https://doi.org/10.1088/1361-6382/ac086d)

Di Valentino, E., et al. 2025, *Phys. Dark Univ.*, 49, 101965, doi: [10.1016/j.dark.2025.101965](https://doi.org/10.1016/j.dark.2025.101965)

Driver, S. P., et al. 2022, *Mon. Not. Roy. Astron. Soc.*, 513, 439, doi: [10.1093/mnras/stac472](https://doi.org/10.1093/mnras/stac472)

Ezquiaga, J. M., & Holz, D. E. 2022, *Phys. Rev. Lett.*, 129, 061102, doi: [10.1103/PhysRevLett.129.061102](https://doi.org/10.1103/PhysRevLett.129.061102)

Fishbach, M., Gray, R., Hernandez, I. M., et al. 2019, *ApJ*, 871, L13, doi: [10.3847/2041-8213/aaf96e](https://doi.org/10.3847/2041-8213/aaf96e)

Gair, J. R., Ghosh, A., Gray, R., et al. 2023, *AJ*, 166, 22, doi: [10.3847/1538-3881/acca78](https://doi.org/10.3847/1538-3881/acca78)

Gallego, J., García-Dabó, C. E., Zamorano, J., Aragón-Salamanca, A., & Rego, M. 2002, *ApJL*, 570, L1, doi: [10.1086/340830](https://doi.org/10.1086/340830)

García-Quirós, C., Colleoni, M., Husa, S., et al. 2020, *PhRvD*, 102, 064002, doi: [10.1103/PhysRevD.102.064002](https://doi.org/10.1103/PhysRevD.102.064002)

Gebhardt, K., Mentuch Cooper, E., Ciardullo, R., et al. 2021, *ApJ*, 923, 217, doi: [10.3847/1538-4357/ac2e03](https://doi.org/10.3847/1538-4357/ac2e03)

Gray, R. 2021, Phd thesis, University of Glasgow, Glasgow, United Kingdom. <https://theses.gla.ac.uk/82438/>

Gray, R., et al. 2020, *PhRvD*, 101, 122001, doi: [10.1103/PhysRevD.101.122001](https://doi.org/10.1103/PhysRevD.101.122001)

Gupta, I. 2023, *MNRAS*, 524, 3537, doi: [10.1093/mnras/stad2115](https://doi.org/10.1093/mnras/stad2115)

Harris, C. R., Millman, K. J., van der Walt, S. J., et al. 2020, *Nature*, 585, 357–362, doi: [10.1038/s41586-020-2649-2](https://doi.org/10.1038/s41586-020-2649-2)

Hawkins, K., Zeimann, G., Sneden, C., et al. 2021, *ApJ*, 911, 108, doi: [10.3847/1538-4357/abe9bd](https://doi.org/10.3847/1538-4357/abe9bd)

Hill, G. J., Lee, H., MacQueen, P. J., et al. 2021, *AJ*, 162, 298, doi: [10.3847/1538-3881/ac2c02](https://doi.org/10.3847/1538-3881/ac2c02)

Holz, D. E., & Hughes, S. A. 2005, *ApJ*, 629, 15, doi: [10.1086/431341](https://doi.org/10.1086/431341)

Huchra, J., & Sargent, W. L. W. 1973, *ApJ*, 186, 433, doi: [10.1086/152510](https://doi.org/10.1086/152510)

Hunter, J. D. 2007, *Computing in Science and Engineering*, 9, 90, doi: [10.1109/MCSE.2007.55](https://doi.org/10.1109/MCSE.2007.55)

Krishna, K., Vijaykumar, A., Ganguly, A., et al. 2023, <https://arxiv.org/abs/2312.06009>

Kuns, K., & Fritschel, P. 2023, A# Strain Sensitivity, Technical Notes, LIGO-T2300041,, <https://dcc.ligo.org/LIGO-T2300041/public> <https://dcc.ligo.org/LIGO-T2300041/public>

Leung, G. C. K., Finkelstein, S. L., Weaver, J. R., et al. 2023, *ApJS*, 269, 46, doi: [10.3847/1538-4365/acf78](https://doi.org/10.3847/1538-4365/acf78)

Madau, P. 1997, *AIP Conf. Proc.*, 393, 481, doi: [10.1063/1.52821](https://doi.org/10.1063/1.52821)

Madau, P., & Dickinson, M. 2014, *ARA&A*, 52, 415, doi: [10.1146/annurev-astro-081811-125615](https://doi.org/10.1146/annurev-astro-081811-125615)

Mastrogiovanni, S., Leyde, K., Karathanasis, C., et al. 2021, *PhRvD*, 104, 062009, doi: [10.1103/PhysRevD.104.062009](https://doi.org/10.1103/PhysRevD.104.062009)

Mastrogiovanni, S., Laghi, D., Gray, R., et al. 2023, *Phys. Rev. D*, 108, 042002, doi: [10.1103/PhysRevD.108.042002](https://doi.org/10.1103/PhysRevD.108.042002)

Mentuch Cooper, E., Gebhardt, K., Davis, D., et al. 2023, *ApJ*, 943, 177, doi: [10.3847/1538-4357/aca962](https://doi.org/10.3847/1538-4357/aca962)

Moore, S. G., Cole, S., Wilson, M., et al. 2025, arXiv e-prints, arXiv:2511.01803, doi: [10.48550/arXiv.2511.01803](https://doi.org/10.48550/arXiv.2511.01803)

Mukherjee, S., Krolewski, A., Wandelt, B. D., & Silk, J. 2024, *ApJ*, 975, 189, doi: [10.3847/1538-4357/ad7d90](https://doi.org/10.3847/1538-4357/ad7d90)

Mukherjee, S., Wandelt, B. D., Nissanke, S. M., & Silvestri, A. 2021, *Phys. Rev. D*, 103, 043520, doi: [10.1103/PhysRevD.103.043520](https://doi.org/10.1103/PhysRevD.103.043520)

Mukherjee, S., Wandelt, B. D., & Silk, J. 2020, *Mon. Not. Roy. Astron. Soc.*, 494, 1956, doi: [10.1093/mnras/staa827](https://doi.org/10.1093/mnras/staa827)

Namikawa, T., Nishizawa, A., & Taruya, A. 2016, *PhRvL*, 116, 121302, doi: [10.1103/PhysRevLett.116.121302](https://doi.org/10.1103/PhysRevLett.116.121302)

Palenzuela, C., Liebling, S. L., Neilsen, D., et al. 2015, *PhRvD*, 92, 044045, doi: [10.1103/PhysRevD.92.044045](https://doi.org/10.1103/PhysRevD.92.044045)

Papovich, C., Shipley, H. V., Mehrtens, N., et al. 2016, *ApJS*, 224, 28, doi: [10.3847/0067-0049/224/2/28](https://doi.org/10.3847/0067-0049/224/2/28)

Poulin, V., Smith, T. L., Karwal, T., & Kamionkowski, M. 2019, *PhRvL*, 122, 221301, doi: [10.1103/PhysRevLett.122.221301](https://doi.org/10.1103/PhysRevLett.122.221301)

Price-Whelan, A. M., Sipőcz, B. M., Günther, H. M., et al. 2018, *The Astronomical Journal*, 156, 123, doi: [10.3847/1538-3881/aabc4f](https://doi.org/10.3847/1538-3881/aabc4f)

Ramsey, L. W., Adams, M. T., Barnes, T. G., et al. 1998, in *Society of Photo-Optical Instrumentation Engineers (SPIE) Conference Series*, Vol. 3352, *Advanced Technology Optical/IR Telescopes VI*, ed. L. M. Stepp, 34–42, doi: [10.1117/12.319287](https://doi.org/10.1117/12.319287)

Riess, A. G., et al. 2022, *ApJL*, 934, L7, doi: [10.3847/2041-8213/ac5c5b](https://doi.org/10.3847/2041-8213/ac5c5b)

Riess, A. G., Li, S., Anand, G. S., et al. 2025, *ApJL*, 992, L34, doi: [10.3847/2041-8213/ae0ad6](https://doi.org/10.3847/2041-8213/ae0ad6)

Salzer, J. J., Gronwall, C., Lipovetsky, V. A., et al. 2000, *AJ*, 120, 80, doi: [10.1086/301418](https://doi.org/10.1086/301418)

Schechter, P. 1976, *Astrophys. J.*, 203, 297, doi: [10.1086/154079](https://doi.org/10.1086/154079)

Schlafly, E. F., & Finkbeiner, D. P. 2011, *ApJ*, 737, 103, doi: [10.1088/0004-637X/737/2/103](https://doi.org/10.1088/0004-637X/737/2/103)

Schlegel, D. J., Finkbeiner, D. P., & Davis, M. 1998, *ApJ*, 500, 525, doi: [10.1086/305772](https://doi.org/10.1086/305772)

Schmidt, M. 1968, *ApJ*, 151, 393, doi: [10.1086/149446](https://doi.org/10.1086/149446)

Schutz, B. F. 1986, *Nature*, 323, 310, doi: [10.1038/323310a0](https://doi.org/10.1038/323310a0)

Schutz, B. F. 2011, *Class. Quant. Grav.*, 28, 125023, doi: [10.1088/0264-9381/28/12/125023](https://doi.org/10.1088/0264-9381/28/12/125023)

Scoville, N., et al. 2007, *ApJS*, 172, 1, doi: [10.1086/516585](https://doi.org/10.1086/516585)

Taylor, S. R., & Gair, J. R. 2012, *PhRvD*, 86, 023502, doi: [10.1103/PhysRevD.86.023502](https://doi.org/10.1103/PhysRevD.86.023502)

Verde, L., Treu, T., & Riess, A. G. 2019, *Nature Astron.*, 3, 891, doi: [10.1038/s41550-019-0902-0](https://doi.org/10.1038/s41550-019-0902-0)

Virtanen, P., Gommers, R., Oliphant, T. E., et al. 2020, *Nature Methods*, 17, 261–272, doi: [10.1038/s41592-019-0686-2](https://doi.org/10.1038/s41592-019-0686-2)

Wysocki, D., Lange, J., & O’Shaughnessy, R. 2019, *PhRvD*, 100, 043012, doi: [10.1103/PhysRevD.100.043012](https://doi.org/10.1103/PhysRevD.100.043012)

Zackay, B., Dai, L., & Venumadhav, T. 2018, <https://arxiv.org/abs/1806.08792>

Zeimann, G. R., Debski, M. H., Schneider, D. P., et al. 2024, *ApJ*, 966, 14, doi: [10.3847/1538-4357/ad35b8](https://doi.org/10.3847/1538-4357/ad35b8)

Zhang, H., Kokubo, M., MacBride, S., et al. 2025, <https://arxiv.org/abs/2508.00291>